Pharmaceutical Research, Vol. 22, No. 7, July 2005 (© 2005)
DOI: 10.1007/s11095-005-6027-4

Research Paper

Identifying and Mapping Surface Amorphous Domains

Stuart Ward,[1] Mark Perkins,[1] Jianxin Zhang,[1] Clive J. Roberts,[2] Claire E. Madden,[1] Shen Y. Luk,[1] Nikin Patel,[1] and Stephen J. Ebbens[1,3]

Received January 28, 2005; accepted April 11, 2005

Purpose. Undesirable amorphous material generation during formulation is implicated in a growing number of pharmaceutical problems. Due to the importance of interfacial properties in many drug delivery systems, it seems that surface amorphous material is particularly significant. Consequently, this study investigates a range of methods capable of detecting and mapping surface amorphous material.
Methods. A micron-sized localized surface domain of amorphous sorbitol is generated using a novel localized heating method. The domain is subsequently investigated using atomic force microscopy (AFM) imaging, nanomechanical measurements, and Raman microscopy 3-D profiling.
Results. AFM phase and height images reveal nanoscale-order variations within both crystalline and amorphous sorbitol domains. Nanomechanical measurements are able to quantitatively distinguish the amorphous and crystalline domains through local Young's modulus measurements. Raman microscopy also distinguishes the amorphous and crystalline sorbitol through variations in peak width. This is shown to allow mapping of the 3-D distribution of the amorphous phase and is hence complementary to the more surface sensitive AFM measurements.
Conclusions. AFM and Raman microscopy map the distribution of amorphous material at the surface of a sorbitol crystal with submicron spatial resolution, demonstrating surface analysis methods for characterizing semicrystalline solids generated during pharmaceutical processing.

KEY WORDS: amorphous content; atomic force microscopy; crystallinity; Raman microscopy.

INTRODUCTION

The issue of amorphous material detection and quantification in pharmaceutical materials has, along with polymorphism, become central during formulation development. This is partly due not only to regulatory requirements (1), but is also driven by the increasing number of formulation problems that can be ascribed to the generation of amorphous material during processing. Commonly employed stages of pharmaceutical manufacture including milling, particle size reduction, and compression provide enough energy to effect changes in active ingredient and excipient crystallinity (2). For example, in formulations where a crystalline active form is targeted, amorphous material often produces unwanted effects. This is due to a variety of factors. Amorphous states can be metastable and, in some cases, allow the nucleation of undesirable polymorphs (3,4). Furthermore, amorphous material may modify dissolution profiles and, in some cases, bioavailability, may alter interactions with other formulation components, and may affect tableting behavior (5). Excipient crystallinity can likewise change formulation performance. An important area where these issues cause significant problem is inhalation devices, in particular, for the most common carrier system, crystalline lactose, in which the presence of amorphous lactose is thought to alter dosage characteristics (6).

Because of the importance of the amorphous issue, it is not surprising that a large array of techniques were applied to address this challenge. In general, most of these methods focused on achieving quantification of overall amounts of amorphous material. This was demonstrated through differential scanning calorimetry, X-ray diffraction, and attenuated total angle reflectance infrared spectroscopy (1). A recent effort to reduce detection levels was driven by increased regulatory rigor and the idea that even low levels of material may exert large effects and explain unwanted batch-to-batch variations. At present, a range of methods including dynamic mechanical analysis and isothermal microcalorimetery (7,8) are vying to provide accurate bulk low-level quantification.

In many cases, it is likely that knowledge of overall levels of amorphous content will not fully explain batch-to-batch variations and other formulation problems. This is because many of the undesirable characteristics introduced by the amorphous phase are due to modifications of interfacial properties (9). Inhalation devices provide an important example in which amorphous material at the surface of an active or excipient causes alteration of adhesion and cohesion, thus changing performance (10). In addition, it seems likely that surface amorphous material may be less

[1] Molecular Profiles Ltd., 8 Orchard Place, Nottingham Business Park, Nottingham, NG8 6PX, UK.
[2] Laboratory of Biophysics and Surface Analysis, School of Pharmacy, The University of Nottingham, Nottingham, NG7 2RD, UK.
[3] To whom correspondence should be addressed. (e-mail: sebbens@molprofiles.co.uk)

stable due to its exposure to moisture and the atmosphere, further adding to the importance of detecting its presence. To address these phenomena, bulk measurements are not sufficient; for example, there is enough amorphous material in a typical 20-μm-sized particle with 1% bulk amorphous content to form a complete overlayer at the surface to a depth of 30 nm. Thicker surface domains can also form if surface coverage is patchy. In this paper, the capability of applying surface sensitive methods to augment bulk determination by allowing detection and imaging of surface amorphous domains is demonstrated.

The model system discussed here is composed of a thin micron-sized domain of amorphous material at the surface of a D-sorbitol (D-glucitol) crystal. Sorbitol is a widely used pharmaceutical excipient, which acts as a sweet-tasting diluent in solid-state formulations and as a stabilizer in suspensions (11). Sorbitol is known to possess at least four crystalline polymorphs and one amorphous form (11). This system was chosen due to the relative stability of the amorphous phase; recrystallization occurs only slowly at low humidity, and the facile formation of amorphous glassy material occurs through quench cooling of a melt (12). The later feature allows generation of small surface amorphous domains through a novel localized heat source composed of a scanning thermal microscope probe (1–2 μm radius) near the crystalline sorbitol surface. The surface analytical methods chosen to characterize the amorphous domains are atomic force microscopy (AFM) and Raman microscopy. AFM imaging has been suggested to allow surface amorphous material in polymers (13) and pharmaceutical systems (14,15) to be imaged through qualitative interpretation of surface topographical and phase images. In topographical mode, surface height variations are recorded, allowing direct visualization of ordered crystalline structures and amorphous areas. In contrast, phase images relate to the energy loss an oscillating probe experiences as it strikes the surface. Consequently, phase imaging can map surface material property variations, such as those that may be present between amorphous and crystalline domains, even when no associated surface height features are present. In addition to phase imaging, the use of nanoindentation AFM measurements to distinguish crystalline and amorphous phases through quantitative determination of local mechanical properties is also demonstrated.

Vibrational spectroscopy has previously been used to determine the degree of crystallinity for carbohydrates (16). In this work, scanning Raman microscopy is applied to allow 3-D mapping of the location of surface amorphous material. Whereas Raman microscopy has a lower lateral spatial resolution compared to AFM (400 nm, cf. < 10 nm), it has the advantage of providing an indication of the depth of amorphous material present and allows direct detection through peak broadening/shifts in the spectra, thus giving the methods complementary benefits.

MATERIALS AND METHODS

A disk of crystalline D-sorbitol (Aldrich, Milwaukee, WI, USA) was prepared using a manual screw thread disc press. A small domain of quench-cooled material was generated at the surface of the sorbitol disc using a 2990 microthermal analyzer (m-TA, TA Instruments, New Castle, DE, USA) equipped with a V-shaped Wollaston thermal probe. Before experiments, the thermal probe was calibrated at a heating rate of 10°C/s following the previously described procedure (17). The thermal probe was then manually positioned to be near the sorbitol disc surface, but not in contact. Subsequently, the probe temperature was then raised to 500°C for a few seconds. This treatment caused the surface temperature to be raised sufficiently by radiative heating to cause localized melting of a small region beneath the probe. This method was developed because the conventional application of a temperature ramp while the probe contacted the sample resulted in the quench-cooled material adhering to the probe and being removed from the sample surface during tip withdrawal. Samples with localized amorphous regions were stored in an evacuated desiccator at room temperature for a maximum duration of a few days before analysis. X-ray diffraction recorded at the end of this storage period showed a spectrum consisting only of a halo, indicating that no detectable recrystallization had occurred. Macroscopic amorphous reference material was generated by melting sorbitol crystals on a hot plate and then allowing it to cool at room temperature.

Scanning electron microscopy (SEM) was carried out using a Leo 1430 VP electron microscope (Zeiss, Hertfordshine, UK). The accelerating voltage was 10 kV at a working distance of 10 mm.

AFM images were recorded on a multimode AFM (Veeco, Santa Barbara, CA, USA) equipped with nanosensor cantilevers (spring constant = 42 N m^{-1}) operating in tapping mode. Resonance frequencies were approximately 270 kHz, the set point ratio used was 0.7 (18), and scan rates were typically 1–2 Hz. AFM force–distance curves, used to derive nanomechanical properties, were collected on the same instrument using stiffer TESP Silicon cantilevers (Veeco). Accurate spring constants for each cantilever used were obtained through the thermal method of calibration (19). In addition to the curves recorded on the sorbitol sample, force–distance curves were obtained from a silicon wafer serving as a hard reference material. The silicon wafer was cleaned in chloroform using an ultrasonic bath (Ultrawave, Cardiff, UK) followed by 30 min in a UV cleaner (Bioforce Nanosciences, Ames, IA, USA). Each data set was recorded using the same cantilever, instrumental adjustments, and experimental parameters.

A comparison of the gradients of the contact region of the force–distance curves between a hard reference and the sample can provide some qualitative indication of the relative hardness of a surface (20). This can be modeled using the Hertz model to obtain a quantitative value of Young's modulus of the surface (20). The model describes the elastic deformation of two homogenous surfaces under an applied load (21) and is often used to model AFM data because it requires little knowledge of parameters such as surface energy (22). The first step in modeling the data is to compare force–distance curves recorded on the sample and the ideally hard reference (silicon) to determine the indentation (δ) of the probe into the sorbitol sample as a function of load.

The value of indentation can be related to the combined elastic modulus of the tip and the sample (K) by:

$$K = \frac{L}{\left(8\,\delta^3 R\right)^{1/2}} \quad (1)$$

where L is the load and R is the radius of the probe. Because the combined elastic modulus contains the elastic modulus for the tip and the sample, an expression containing the E_s, the elastic modulus of the sample can be obtained:

$$K = \frac{4}{3}\left(\frac{1-\nu_t^2}{E_t} + \frac{1-\nu_s^2}{E_s}\right)^{-1} \quad (2)$$

where ν_t and ν_s are the Poisson's ratio of the tip and the sample, respectively. The values of ν_t and E_t are known, and because $\nu_t \approx 1$, the first bracketed term of Eq. (2) reduces to zero to produce Eq. (3):

$$E_s = \frac{3K(1-\nu_s)^2}{4} \quad (3)$$

Combining Eqs. (1) and (3) derives:

$$E_s = \frac{3L(1-\nu_s^2)}{4(8\delta^3 R)^{1/2}} \quad (4)$$

Poissons ratio is difficult to determine accurately for the sample, and so in this instance we assume ν_s = 0.33 for sorbitol (midrange for polymers) (21,22). R is deduced from the tip profile determined from an image recorded on a porous aluminum sample (Agar Scientific, Essex, UK), in this case 10 nm.

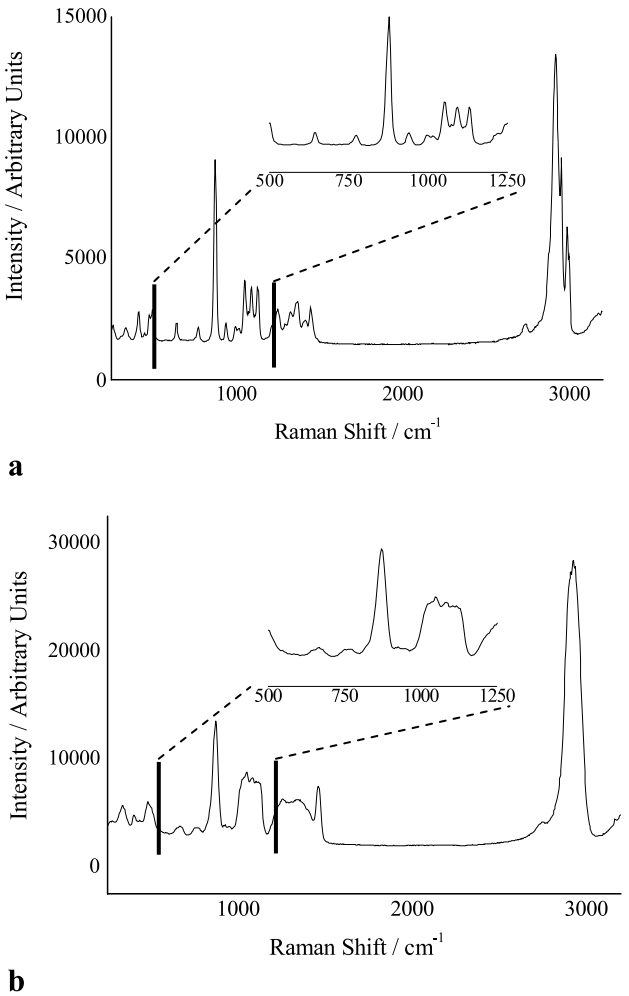

Fig. 1. Raman spectra: (a) crystalline sorbitol and (b) quench-cooled glassy sorbitol.

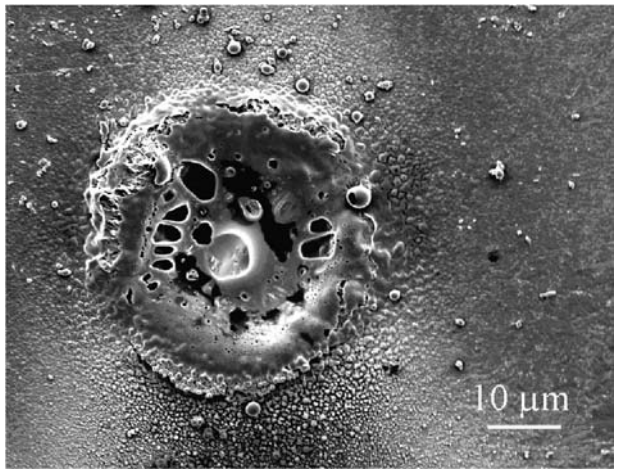

Fig. 2. Scanning electron micrograph of a quench-cooled domain generating using the scanning thermal microscope probe.

Raman spectra were recorded with a CRM200 confocal Raman microscope (Witec, Ulm, Germany), equipped with a 532-nm Nd:YAG laser. The laser excitation was focused using a ×100 objective (Nikon, Kinston upon Thames, NA 0.90) and the scattered light was collected using a 180° back-scatter regime, with the laser line intensity being suppressed using an edge filter. The Stokes shifted Raman scatter was dispersed using a 600 groove/mm grating onto a Peltier cooled Andor charged-coupled device (CCD, Andor, Belfast, UK) to capture a spectrum. Under these conditions, the spectral resolution was 8 cm^{-1} and the lateral resolution was 500 nm.

Chemical maps were constructed through the use of a serial imaging process, which involves the acquisition of spectra at defined points within an array (a set of equally spaced points with predefined spatial dimensions). Specific characteristic Raman peaks from the spectra were reprocessed to produce the Raman image.

RESULTS

Figure 1a and b shows the Raman spectra for crystalline and glassy quench-cooled sorbitol, respectively. Comparison of the spectra reveals that the glassy state is characterized by broader peaks and loss of fine spectral structure, features that are typical of a disordered amorphous state (16). In particular, the broadening of the peak at 878 cm^{-1} assigned to the C–C–O stretch showed an increase in full-width at half maximum from 15 (crystalline) to 34 cm^{-1} (glassy) and so provided an intensity-independent method of mapping for sorbitol degree of crystallinity. In addition, the absence of any new peaks shows that the heating does not induce chemical degradation.

The topography of a typical amorphous domain is shown in an SEM micrograph (Fig. 2). It is apparent that localized exposure to the thermal radiation from the scanning thermal probe has generated a roughly circular region of quenched-cooled molten material, in this case around 30 μm in diameter. The texture of the material in this modified region appears smoother and glassy compared to the surroundings.

It is noted that some additional topography is generated during the heating process, for example, the appearance of some cavities. However, by careful selection of the analysis region for subsequent experiments, these features could be avoided. By varying the probe–sample distance during the localized melting event it was possible to alter the size of the melted domain accordingly.

A more detailed investigation was possible using AFM topographic and phase imaging both outside and inside of a typical modified localized domain, Fig. 3a and b, respectively. The topography of the unmodified, crystalline regions is composed of columnar objects with a mean length of 0.8 μm and width of 0.2 μm (Fig. 3a). The corresponding phase image highlights the morphology and reveals additional banding structures running normal to the needles' long axis. Inside the modified domains the surface topography is much smoother (Fig. 3b). Some small circular raised domains are present and are accentuated in the phase images.

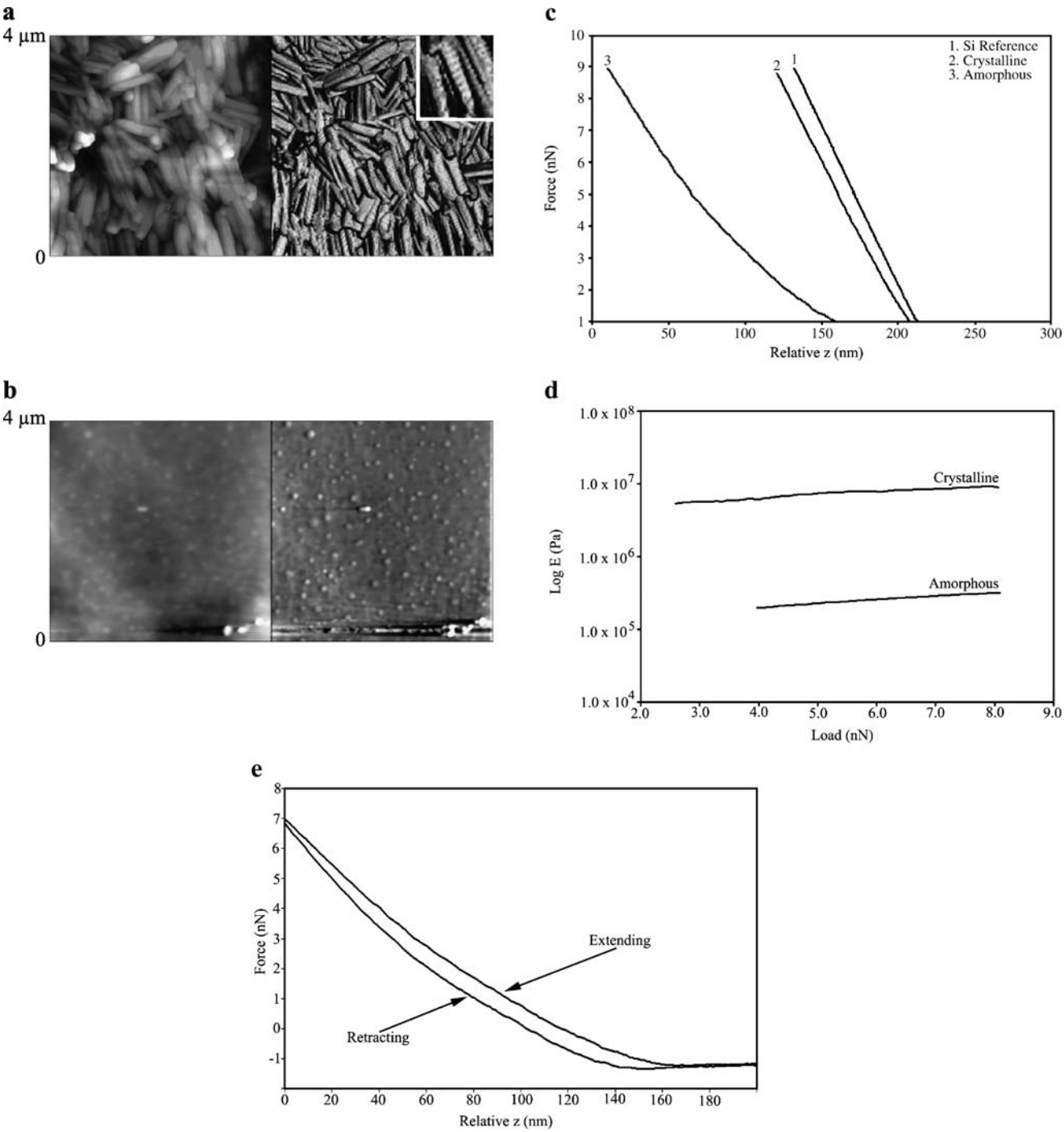

Fig. 3. (a) Atomic force micrograph of unmodified sorbitol (height image on left pane; phase image on right pane); inset highlights banding structure. (b) Atomic force micrograph within a quench-cooled domain of sorbitol. (c) Nanoindentation curves for the crystalline and amorphous domains. (d) Load dependence of nanoscale Young's modulus. (e) Force curve from the amorphous domain.

Nanoindentation measurements were also performed in an attempt to distinguish the crystalline and glassy material. Fig. 3c displays typical approach force–distance curves recorded on amorphous and crystalline sorbitol regions and a reference curve recorded on a hard silicon substrate. Qualitatively, it is apparent that the crystalline and amorphous regions have different nanoindentation profiles. At a given applied load, the deflection of the tip is greater in the amorphous region than in the crystalline domain, indicating a greater indentation and hence softer material. By applying the indentation model discussed above, it is possible to quantify Young's modulus from the nanoindentation curves as a function of load (Fig. 3d). It is apparent that the Young's modulus values for the crystalline phase are greater than those for the amorphous phase at all loads. For example at a load of 8 nN, the Young's modulus values range from 28 to 31 (SD =

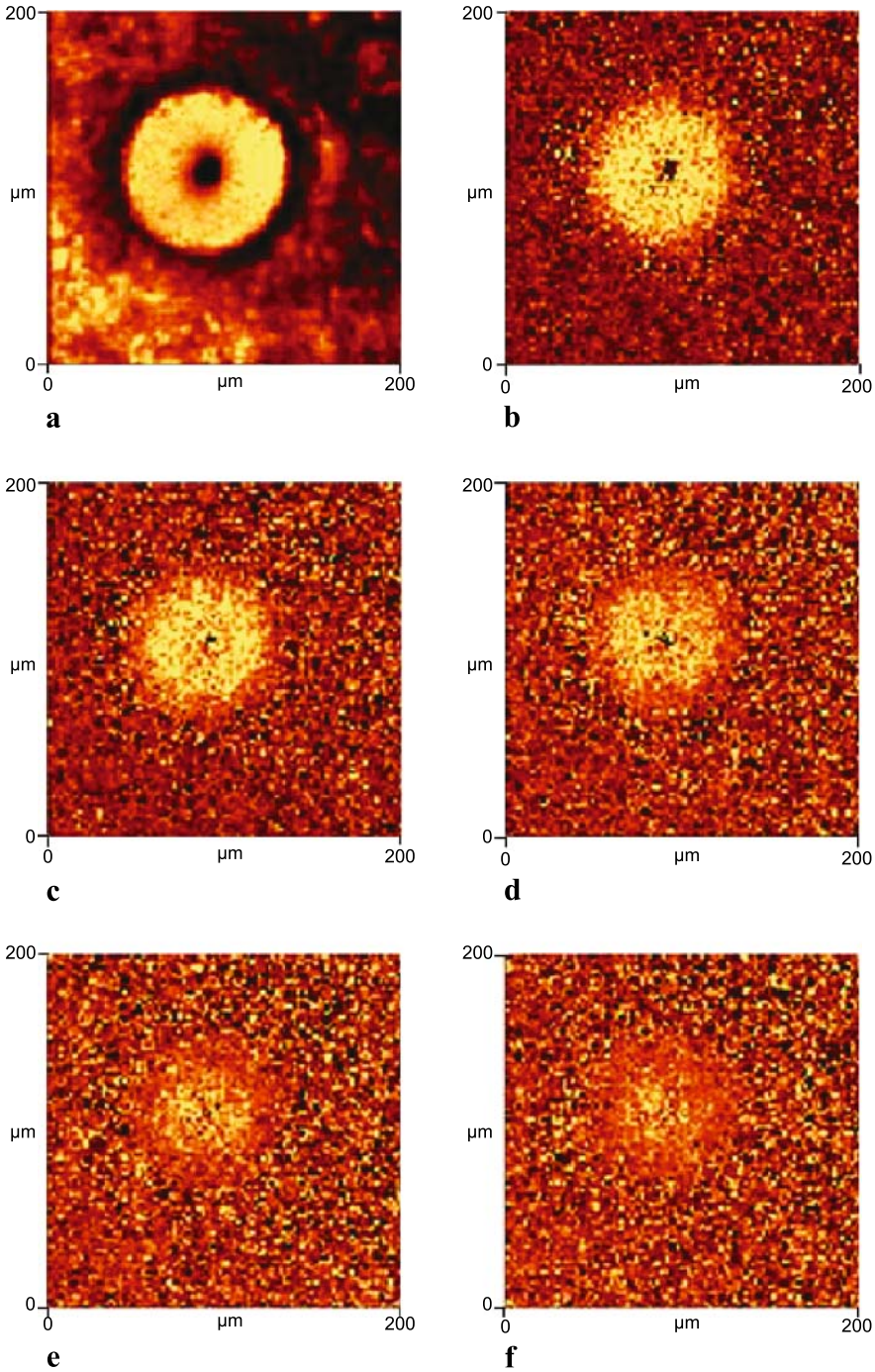

Fig. 4. Raman images of a quench-cooled sorbitol domain. (a) Peak intensity 850–900 cm^{-1}, $z = 0$ μm. (b) Peak width 850–900 cm^{-1}, $z = 0$ μm. (c) Peak width 850–900 cm^{-1}, $z = -5$ μm. (d) Peak width 850–900 cm^{-1}, $z = -10$ μm, (e) Peak width 850–900 cm^{-1}; $z = -15$ μm; (f) Peak width 850–900 cm^{-1}, $z = -20$ μm.

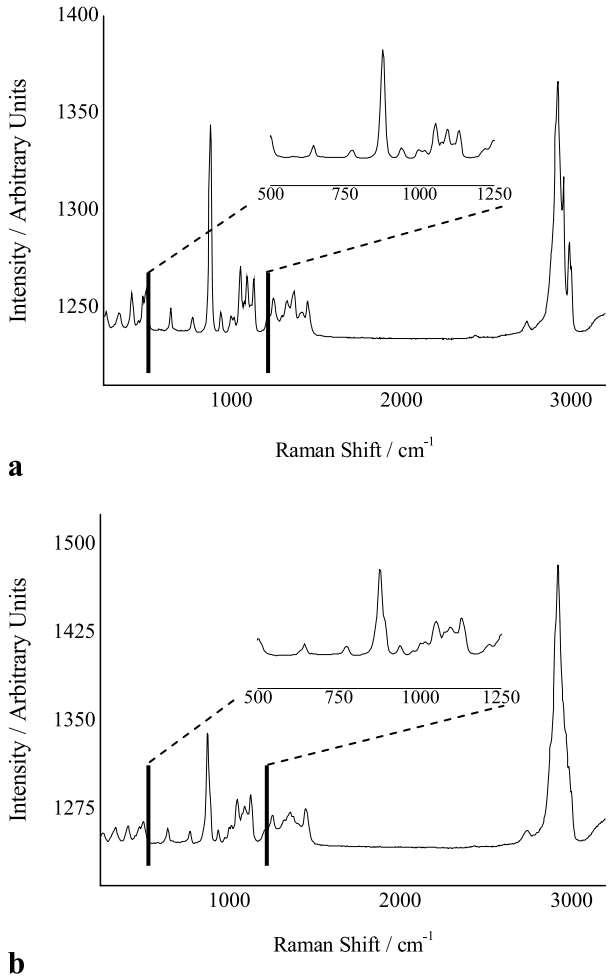

Fig. 5. Reconstructed average Raman spectra from the quench-cooled domains and the surrounding crystalline regions identified in Fig. 4: (a) Crystalline (b) quench cooled.

0.9) MPa. In contrast, the crystalline region's modulus values range from 85 to 93 MPa (SD = 2.4). The greater spread in the data recorded from the crystalline material is likely to be due to its polycrystalline nature. For an ideal elastic material Young's modulus should not vary with load; however, for these materials, Young's modulus is observed to increase with load, suggesting a viscoelastic/plastic deformation. A further difference between the amorphous and crystalline domains is revealed by comparing the approach and retract force distance data in the contact region. Curves recorded in the crystalline region show no hysteresis, i.e., approach and retract curves completely overlap (data not shown). However, the amorphous phase displays an appreciable hysteresis between loading and unloading behavior (Fig. 3e).

As discussed above, full-width at half maximum widths of the sorbitol 878 cm^{-1} peak in Raman spectra can be used to distinguish crystalline and amorphous regions independent of peak intensity. This has been used to image the location of amorphous and crystalline material in a series of confocal stacks (Fig. 4). The 850–900 cm^{-1} peak intensity image is included because it gives a good representation of the toroidal shape of the modified region, Fig. 4a. It should be noted that the domain chosen for Raman analysis is larger (approximately 80 μm diameter) compared to the sample used for SEM, exhibiting the varying sizes and morphologies produced by the localized thermal treatment method. Figures 4b–f display confocal maps recorded at increasing depths based on the width of the 878 cm^{-1} peak. In this image series, brighter contrast indicates a wider peak and so greater amorphous content. A concentric ring of bright contrast due to amorphous phase is visible in the first crystallinity map. As the confocal plane is lowered into the sample, the intensity of the circular domain diminishes, and its diameter reduces, with little contrast visible in the final section, recorded 20 μm below the initial surface image. Raman spectra were summed and averaged from the regions identified as being crystalline and amorphous in the above stacked images (Fig. 5). This result is consistent with the spectra recorded from the macroscopic reference samples. Material outside the modification appears to be wholly crystalline, whereas the modified region exhibits partial broadening and loss of fine spectral structure, indicating an increased amorphous content. In addition, there are no additional peaks introduced into the spectra because of the thermal treatment. These data confirm that the novel localized thermal treatment does produce quench-cooled amorphous material without degradation of the sorbitol.

DISCUSSION

Using AFM morphological imaging it is possible to qualitatively distinguish the surface crystalline and amorphous regions. In addition to the morphological differences, some interesting details are revealed in the accompanying phase images. The banding seen across some of the crystalline needles is likely to be due to lamellae structure (Fig. 3a). It is known that phase imaging can distinguish ordered and disordered regions within crystal structures by virtue of their differing mechanical responses (23). Ordered regions such as lamellae have a higher density and are harder, producing less energy loss per tapping mode cycle, and so a lower phase shift (brighter), whereas disordered regions such as lamellae boundaries cause greater energy loss, and so greater phase shift, and appear darker in images (24).

Phase imaging also reveals fine structures within the amorphous domains. It is possible that the brighter regions are small ordered regions, indicating the amorphous domain may retain some small crystallites, or that these have formed during sample storage. Although these observations show that subtle differences in surface order can be detected using AFM, the observations rely on qualitative interpretation of the recorded images.

The ability to distinguish surface crystalline and amorphous phases by virtue of their indentation behavior removes the need for qualitative interpretation of AFM images to locate the two phases. For the future, through use of the force–volume method it should be possible to generate spatial maps of local Young's modulus variations and so visualize the surface distribution (25). Here, an amorphous domain of 20-μm depth has been shown to behave similarly to a macroscopic sample. The depth of analysis achieved by this method will be related to the maximum indentation, in this case 13 nm for crystalline material and 122 nm for amorphous material. In other studies, it has been shown that soft overlayers as thin as 50 nm can be distinguished from underlying

stiffer material (26). Hence, this approach seems to provide a method capable of detecting small amounts of surface amorphous material and assessing the spatial distribution.

The load dependence of the measured Young's modulus suggests that neither material is deforming completely elastically. This may be partly due to the high stress regime applied by the highly curved probe tip (radius 10 nm). It may emerge that Young's modulus *vs.* load curves provide a useful method for categorizing deformation behavior. In addition, the contact region of the force curves provides additional information about deformation behavior. The observed hysteresis for the amorphous material suggests that a time-dependent reorganization is occurring during the unloading cycle.

Raman mapping provides a complementary tool capable of distinguishing crystalline and amorphous regions, as vibrational bands are altered by a molecules physical environment. In this case, confocal Raman microscopy reveals the distribution of amorphous sorbitol material within the thermally modified region. This type of experiment was not possible with AFM due to the large vertical height differences across the sample. The first confocal slice indicates the amorphous material forms a ring at the surface, with the darker central region resulting from a dip in the topography of the treated region, apparent in the SEM images, and a resulting lower Raman signal. The deeper slices reveal that the amorphous domain is cone shaped, with a maximum depth of roughly 20 μm. This profile qualitatively relates to the heat transfer from the scanning thermal probe tip into the sorbitol.

CONCLUSION

Both atomic force microscopy and Raman microscopy offer the ability to identify and map surface amorphous domains. AFM allows nanoscale differences in molecular order to be determined through phase imaging. This ability could prove valuable in investigating the distribution of amorphous material at the surface of pharmaceutical ingredients. AFM mechanical measurements have been shown to distinguish amorphous and crystalline domains by virtue of quantitative differences in nanoscale Young's modulus. Because surface mechanical properties are known to affect pharmaceutical properties such as behavior during tableting and interparticulate adhesion, this screening technique may help solve batch-to-batch variation problems. Raman microscopy provides a complementary method that is able to provide depth and lateral information about amorphous material distribution on the microscale. The ability to determine the 3-D distribution of amorphous material within a crystalline matrix may allow insights into recrystallization phenomena in real pharmaceutical components. Until now, attempts to measure low levels of amorphous content have focused on model systems comprising appropriately blended pure amorphous and pure crystalline particles. However, it is more likely that pharmaceutical processing produces semicrystalline particles containing both amorphous and crystalline domains. It has been speculated that such particles could respond differently to the blended material when characterized using conventional methods such as isothermal calorimetry (27), highlighting an area where the 3-D capabilities of Raman may provide illumination. Although a pharmaceutical excipient was studied here, these methods would apply equally well to detecting amorphous content in active ingredients; for example, Raman spectroscopy has previously been used to determine crystallinity in a model active (28).

REFERENCES

1. D. Giron, M. Mutz, and S. Garnier. Solid state pharmaceutical compounds: impact of the ICH Q6 guideline on industrial development. *J. Therm. Anal. Calorim.* **77**:709–747 (2004).
2. G. Brittain. Effects of mechanical processing on phase composition. *J. Pharm. Sci.* **91**:1573–1579 (2002).
3. J. Pirttimäi, E. Laine, J. Ketolainen, and P. Paronen. Effect of grinding and compression on crystal structure of anhydrous caffeine. *Int. J. Pharm.* **95**:93–99 (1993).
4. A. Bauer-Brandl. Polymorphic transitions of cimetidine during manufacture of solid dosage forms. *Int. J. Pharm.* **140**:195–206 (1996).
5. D. Singhal and W. Curatolo. Drug polymorphism and dosage form design: a practical perspective. *Adv. Drug Deliv. Rev.* **56**:335–347 (2004).
6. M. Murtomaa, V. Mellin, P. Harjunen, T. Lankinen, E. Laine, and V.-P. Lehto. Effect of particle morphology on the triboelectrification in dry powder inhalers. *Int. J. Pharm.* **282**:107–114 (2004).
7. G. Buckton, P. Darcy, D. Greenleaf, and P. Holbrook. The use of isothermal microcalorimetry in spray-dried salbutamol sulphate. *Int. J. Pharm.* **116**:113–118 (1995).
8. G. Buckton and P. Darcy. The influence of additives on the recrystallisation of amorphous spray dried lactose. *Int. J. Pharm.* **121**:81–87 (1995).
9. G. Buckton. Characterisation of small changes in the physical properties of powders of significance for dry powder inhaler formulations. *Adv. Drug Deliv. Rev.* **26**:17–27 (1997).
10. V. Bérard, E. Lesniewska, C. Andrés, D. Pertuy, C. Laroche, and Y. Pourcelot. Affinity scale between a carrier and a drug in DPI studied by atomic force microscopy. *Int. J. Pharm.* **247**:127–137 (2002).
11. R. C. Rowe, P. J. Shesky, and P. J. Weller. *Handbook of Pharmaceutical Excipients*, Pharmaceutical Press, London, 2003.
12. R. A. Talja and Y. H. Roos. Phase and state transition effects on dielectric, mechanical and themal properties of polyols. *Thermochim. Acta* **380**:109–121 (2001).
13. J. X. Zhang, A. J. Busby, C. J. Roberts, X. Y. Chen, M. C. Davies, S. J. B. Tendler, and S. M. Howdle. Preparation of a poly(methyl methacrylate)/ultrahigh molecular weight polyethylene blend using supercritical carbon dioxide and the identification of a three-phase structure: an atomic force microscopy study. *Macromolecules* **35**:8869–8877 (2002).
14. R. Price and P. M. Young. Visualization of the crystallisation of lactose from the amorphous state. *J. Pharm. Sci.* **93**:155–164 (2004).
15. D. Mahlin, J. Berggren, G. Alderborn, and S. Engström. Moisture-induced crystallisation of spray-dried amorphous lactose particles studied by atomic force microscopy. *J. Pharm. Sci.* **92**:29–37 (2004).
16. L. S. Taylor, A. C. Williams, and P. York. Particle size dependant molecular rearrangements during the dehydration of trehalose dehydrate-*in situ* FT-Raman spectroscopy. *Pharm. Res.* **15**:1207–1214 (1998).
17. J. X. Zhang, C. J. Roberts, K. M. Shakesheff, M. C. Davies, and S. J. B. Tendler. Micro- and macrothermal analysis of a bioactive surface-engineered polymer formed by physical entrapment of poly(ethylene glycol) into poly(lactic acid). *Macromolecules* **36**:1215–1221 (2003).
18. G. Bar, Y. Thomann, R. Brandsch, H. J. Cantow, and M. H. Whangbo. Factors affecting the height and phase images in tapping mode atomic force microscopy. Study of phase-separated polymer blends of poly(ethene-*co*-styrene) and poly(2,6-dimethyl-1,4-phenylene oxide). *Langmuir* **13**:3807–3812 (1997).
19. R. Levy and M. Maaloum. Measuring the spring constant of atomic force microscope cantilevers: thermal fluctuations and other methods. *Nanotechnology* **13**:33–37 (2002).

20. M. Radmacher. Measuring the elastic properties of biological samples with the AFM. *IEEE Eng. Med. Biol. Mag.* **16**:47–57 (1997).
21. A. N. Round, B. Yan, S. Dang, R. Estephan, R. E. Stark, and J. D. Batteas. The influence of water on the nanomechanical behavior of the plant biopolyester cutin as studied by AFM and solid-state NMR. *Biophys. J.* **79**:2761–2767 (2000).
22. E. A-Hassan, W. F. Heinz, M. D. Antonik, N. P. D'Costa, S. Nageswaran, C. A. Schoenenberger, and J. H. Hoh. Relative microelastic mapping of living cells by atomic force microscopy. *Biophys. J.* **74**:1564–1578 (1998).
23. S. J. Ebbens and J. P. S. Badyal. Surface enrichment of fluorochemical-doped polypropylene films. *Langmuir* **17**:4050–4055 (2001).
24. J. P. Cleveland, B. Anczykowski, A. E. Schmid, and V. B. Elings. Energy dissipation in tapping-mode atomic force microscopy. *Appl. Phys. Lett.* **72**:2613–2615 (1998).
25. M. Heubeger, G. Dietler, and L. Schalapbach. Mapping the local Young's modulus by analysis of the elastic deformations occurring in atomic force microscopy. *Nanotechnology* **5**:12–23 (1994).
26. J. Domke and M. Radmacher. Measuring elastic properties of thin polymer films with the atomic force microscope. *Langmuir* **14**:3320–3325 (1998).
27. S. E. Dilworth, G. Buckton, S. Gaisford, and R. Ramos. Approaches to determine the enthalpy of crystallisation, and amorphous content of lactose from isothermal calorimetric data. *Int. J. Pharm.* **284**:83–94 (2004).
28. L. S. Taylor and G. Zografi. The quantitative analysis of crystallinity using FT-Raman spectroscopy. *Pharm. Res.* **15**:755–761 (1998).